IEEE Access
Multidisciplinary ⋮ Rapid Review ⋮ Open Access Journal

Received March 16, 2022, accepted March 29, 2022, date of publication April 1, 2022, date of current version April 7, 2022.

Digital Object Identifier 10.1109/ACCESS.2022.3164184

Infrared Dim and Small Target Detection Algorithm Combining Multiway Gradient Regularized Principal Component Decomposition Model

ANQING WU[1], XIANGSUO FAN[1], HUAJIN CHEN[1], LEI MIN[2], AND ZHIYONG XU[2]
[1]School of Electrical, Electronic and Computer Science, Guangxi University of Science and Technology, Liuzhou 545006, China
[2]Institute of Optics and Electronics, Chinese Academy of Sciences, Chengdu 610209, China

Corresponding authors: Xiangsuo Fan (100002085@gxust.edu.cn) and Lei Min (minlei1986@163.com)

This work was supported in part by the Guangxi Natural Science Foundation under Grant 2021GXNSFBA075029, in part by the National Natural Science Foundation of China under Grant 62001129, and in part by the Guangxi Science and Technology Base and Talent Project under Grant AD19245130.

ABSTRACT In complex non-smooth backgrounds, infrared dim and small target targets generally have lower energy and occupy fewer pixels, and are easily swamped by clutter. To improve the detection capability of dim and small targets in non-smooth scenes, this paper proposes a new dim and small target detection method combining multidirectional gradient difference regularization principal component decomposition model. The method first establishes a new gradient difference regularization to constrain the low-rank subspaces of different image components, then construct a gradient difference regularization-based principal component decomposition model (GDR-PCD), and finally decomposes the model using the overlapping directional multiplier method to obtain the background impedance. The experimental results show that the method performs better in all six sequential image scenes than the traditional algorithm. Furthermore, the detection results verify the algorithm's effectiveness in this paper.

INDEX TERMS Infrared dim and small target detection, principal component decomposition model, gradient difference regularization principal component decomposition model, overlapping directional multiplier method.

I. INTRODUCTION

Infrared dim and small target detection have numerous military applications, including guidance, antimissile, and early warning. In the past decades, with the research of many scholars at home and abroad, infrared dim and small target detection has achieved good results in engineering applications, mainly in two aspects, detection before tracking (DBT) [1]–[4] and tracking before detection (TBD). DBT is a classical small target detection algorithm. To achieve target tracking, this method is used to calculate the detection threshold of a single-frame based on the detection probability and false alarm probability, then each frame is segmented, the single-frame detection result is obtained by the detection threshold, and the detection results of multiple frames are correlated with the target motion trajectory. The flow of the algorithm is shown in Fig. 1.

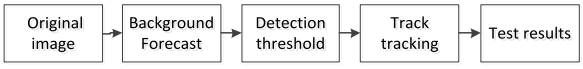

FIGURE 1. DBT algorithm process.

The DBT method has an intuitive process and a simple algorithm. The detection effect is performance good when the signal-to-noise ratio is high (>10 dB), but it will fail in complex backgrounds with low signal-to-noise ratio [5], because when the signal-to-noise ratio is low, the grayscale values of the target signal and background image do not differ considerably. The calculated detection threshold cannot segment the target signal and background image, resulting in poor detection. The current representative algorithms of DBT are pipeline filtering algorithms. Xie *et al.* [6] proposed

The associate editor coordinating the review of this manuscript and approving it for publication was Gustavo Callico.

a method to obtain the amount of interframe jitter using normalized mutual correlation function for interframe block-matching and using normalized mutual information to evaluate the similarity of matching regions and designed a pipeline filtering method with anti-jitter performance. Dong *et al.* [7] proposed a proposed a small target detection method combining a modified visual attention model (VAM) with an anti-vibration pipe filtering algorithm, which first adaptively selects the best modality to compute the saliency map based on the background smoothness evaluation; then automatically extracts suspicious targets and suppresses background clutter based on a designed local saliency singularity evaluation strategy; and finally anti-vibration pipeline filtering method based on multi-frame clutter elimination is adopted to remove clutter and determine the real target. It can significantly improve the success rate and efficiency of the IR imager for targets under different weather conditions. Zhang *et al.* [8] studied a small target detection method that combines local peak detection technique and pipeline filtering algorithm. The method first extracts the suspicious targets in the image using the local peak detection technique, then excludes most of the interference in the suspicious targets according to the adaptive domain value method, and finally removes the remaining interference using the pipeline filtering method to obtain the real targets. Although several researchers have improved the pipeline filtering methods, the detection of moving targets in complex background environments remains poor. The TBD method is mainly used to detect dim and small targets in images with low signal-to-noise ratios, but it does not determine the presence or absence of targets in single-frame images. However, it makes assumptions about targets and backgrounds through a priori information of images. Then, it combines the information of multi-frame images to make decisions to detect dim and small targets in infrared image. The TBD method is divided into three steps (Fig. 2): first, background suppression, which separates the low- and high-frequency parts of the infrared image through filtering to improve the signal-to-noise ratio (SNR) and suppress the low-frequency background clutter in the original image as much as possible; second, suspicious target tracking, which uses the motion information derived from the original image; and third, suspicious target detection, which uses the motion information derived from the original image. Third step uses the continuity of the target motion and the consistency of the trajectory in the sequence image to further exclude false targets and detect the real targets among the candidate targets. TBD algorithms include the 3D matched filtering algorithm, projection transformation algorithm, dynamic programming algorithm, and higher-order correlation method.

Reed *et al.* [9] first applies three-dimensional matched filtering to the field of small target detection. The method first obtains SNR through two-bit spatial matched filtering, then accumulates the obtained signal-to-noise ratio by combining with one-dimensional time, and finally determines the real target by the magnitude of the signal-to-noise ratio, which has a considerable limitation and can only hold when the target

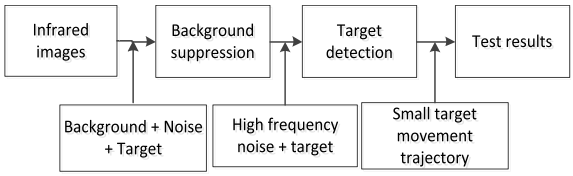

FIGURE 2. Infrared dim and small target TBD algorithm design flow.

intensity remains reasonably constant throughout the filter integration time. On this basis, Yan *et al.* [10] combined the acceleration motion model with three-dimensional matched filtering and proposed a motion target indication algorithm based on a linear variable coefficient difference equation. Although several three-dimensional matched filtering algorithms are optimized to reduce the computational complexity of this algorithm, the computation will become more complex and tedious for motion targets with velocity mismatch, which require more intensive velocity direction filters. Gong *et al.* [11] proposed a multi-scale random projection-based background suppression method for infrared images; the main idea is to separate the background and target from the original infrared image using a non-down sampling pyramid transform, and then use random projection to further suppress other cluttered backgrounds and enhance the target. The projection transform decreases the amount of computation and storage in the detection process but at the expense of detection performance; especially in the case of low SNR or fast target motion, the projection transform-based small target detection algorithm is less effective. Guo *et al.* [12] studied a dynamic planning method based on parallel computing, which divides the detection area into several parts and performs energy integration in parallel for each part to reduce the computational complexity of each part. The detection efficiency of the target and the operation efficiency of the method are improved. However, because the algorithm needs to search for all possible target trajectories, it still requires a huge amount of computation. Hence, the engineering application of such a method is difficult. Fan *et al.* [13] uses Poisson distribution to preprocess the images and combines with higher-order accumulation to extract further dim and small targets, thus achieving good detection results. However, the change algorithm requires multiple frames for accumulation, which consumes a longer time.

In the field of machine learning small target detection, many scholars have achieved good results. Gao *et al.* [14] chunks the image and determines the rank of each image block, and his proposed algorithm is good at preserving the low-rank characteristic of the image block compared with the rank of the original image, but it also has some drawbacks. The rank of the image block is closely related to the size of the sliding window division and the step size; therefore, selecting the step size parameter in practical application is inappropriate; moreover, when the division of an image block is in the non-smooth edge, the number of nonzero singular values of the block is high, making it difficult to satisfy the low-

rank assumption theory. The detailed information regarding the image (such as changing clouds, fluctuating waves, etc.) will be lost in the process of background recovery, resulting in a blurred background and the high false alarm rate of the obtained difference map. Thus, Liu and Peng [15] proposes a guided image filtering infrared image model instead of the commonly used IPI model to achieve the effect of reducing the computational complexity and suppressing the noise signal, while using the kernel parametric and L1 parametric to constrain the background and target components. Wang *et al.* [16] analyzes the background structure based on a single subspace to construct a multi-subspace dictionary and uses it to estimate the background image to achieve dim and small target detection. The algorithm has good detection performance in the case of large differences in the background of infrared images. However, when the background of the infrared image is in the undulating and variable edge region, the constructed dictionary is unable to provide a complete description of the background image, thus affecting the detection performance. Pang *et al.* [17] proposes a new spatio-temporal saliency method, which first calculates the spatial variance saliency mapping on the spatial domain and the temporal gray saliency mapping on the temporal domain, and then combines the spatial and temporal salinity maps to obtain the target, and finally achieves better detection results. Sun *et al.* [18] combines the correlation of time and space domains and introduces multi-subspace into the tensor domain. The tensor dictionary constructed based on the idea of multi-subspace can effectively preserve the background features of infrared images. However, the algorithm loses the target information in the non-smooth background, affecting the detection effect. Cao *et al.* [19] proposed a mode-k1 k2 expansion tensor tube rank (METTR) based on the IPT model, which enables deep mining of tensor modal structure information through the METTR norm. Wang *et al.* [20] constructs a nonoverlapping patch spatial–temporal tensor (NPSTT) model by correlating local and global information on the spatio-temporal domain of sequence images, while combining tensor capped nuclear norm (TCNN) to separate target and background images. Kong *et al.* [21] expands the tensor rank to tensor fiber rank by multimodal t-SVD, while using hyper-total variation (HTV) as a regularization term to achieve constraints on the background and retention of target information. Pang *et al.* [22] proposed a low-rank and sparse decomposition method based on greedy bilateral decomposition, which analyzes the information of the motion target in the sequence image and treats the target as the sparse part, while the low-rank part is approximated by using the bilateral factorization strategy to greatly improve the operation efficiency of the algorithm. Wang *et al.* [23] introduced isotropic all-variance theory on the basis of IPI model, which makes full use of the local autocorrelation of the background image through IPI model and achieves joint regularization on the basis of the original principal component tracking model with the help of isotropic all-variance, which well preserves the background information of the image and thus establishes a good background model,

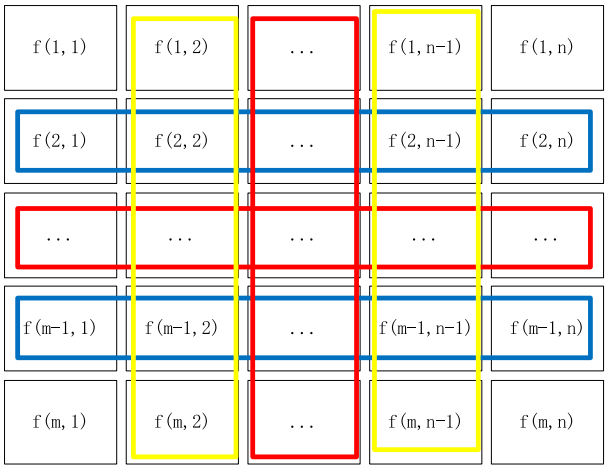

FIGURE 3. Schematic diagram of the gradient difference calculation method.

but the all-variance theory used in this algorithm only relies on the null domain local correlation of the image block for background constraint, and there is insufficient information utilization, and when the background is in dynamic change (e.g., illumination change, non-smooth background), there are some edge contour false target points in the difference image.

In this paper, based on the literature [22], we propose a dim and small target detection method combining multidirectional gradient difference regularization principal component decomposition model, and this paper improves the problem that isotropic full variance only uses the difference between left and right neighboring pixels without considering the overall information of the upper and lower neighborhood of the image, and replaces the isotropic full variance regularization factor with a new gradient difference regularization factor, so that the algorithm obtains a better background constraint effect in complex scenes. This study makes two major contributions: first, it establishes a new anisotropic regularization factor by the difference between neighboring vectors in different directions, which efficiently uses information in the neighborhood space to further constrain the low-rank characteristics of image sub-blocks; second, construct a gradient difference regularization-based principal component decomposition model (GDR-PCD). Consequently, the model can better decompose each image component and effectively extract dim and small targets in each experimental scene.

II. GRADIENT DIFFERENCE REGULARIZATION

The anisotropic diffusion algorithm is used in the literature [24] for dim and small target detection, which uses the gradient difference in each direction to distinguish between the target and the background and is more effective for dynamic changes or large span backgrounds. Thus, the paper proposes a gradient difference regularization method combined with the idea of anisotropy, and the gradient difference regularization factor is defined by the gradient difference between

row and column vectors combined with the diffusion function (Fig. 3):

According to Fig. 3, the horizontal gradient difference is obtained by making the difference between an adjacent horizontal vector in the image matrix and summing the resulting gradient difference to obtain the average value, and the vertical gradient difference is obtained by making the difference between adjacent vertical vector and summing the resulting gradient difference to obtain the average value, as defined by the following equation:

$$\begin{cases} \Delta f(X_U) = (\sum_{j=1}^{n-1} |f(i,j) - f(i-step,j)|)/n - 1 \\ \Delta f(X_D) = (\sum_{j=1}^{n-1} |f(i,j) - f(i+step,j)|)/n - 1 \\ \Delta f(Y_L) = (\sum_{i=1}^{m-1} |f(i,j) - f(i,j-step)|)/m - 1 \\ \Delta f(Y_R) = (\sum_{i=1}^{m-1} |f(i,j) - f(i,j+step)|)/m - 1 \end{cases} \tag{1}$$

In (1), f(i,j) denotes the gray value of the image element at position (i,j), step denotes the set step, m and n denote the rows and columns of the image matrix, respectively, and Δf(x) denotes the gradient difference. The anisotropic diffusion function is established and calculated by [18]:

$$S(\nabla f) = \frac{1}{1 + \frac{1}{1+t\times\frac{\nabla f}{k}}} \tag{2}$$

The regularization factor is constructed by combining the anisotropic diffusion function, which is defined by the following equation:

$$\begin{cases} S_U = 1/[1 + 1/(1 + t \times \Delta f(X_U)/K)] \\ S_D = 1/[1 + 1/(1 + t \times \Delta f(X_D)/K)] \\ S_L = 1/[1 + 1/(1 + t \times \Delta f(Y_L)/K)] \\ S_R = 1/[1 + 1/(1 + t \times \Delta f(Y_R)/K)] \\ GD(X) = \sum_{i=1}^{m-1}\sum_{j=1}^{n-1} \left\{ \begin{array}{l} |f(i,j) - f(i-step,j)| \times \frac{S_U}{2} \\ + |f(i,j) - f(i+step,j)| \times \frac{S_D}{2} \end{array} \right\} \\ \qquad + \sum_{j=1}^{n-1}\sum_{i=1}^{m-1} \left\{ \begin{array}{l} |f(i,j) - f(i,j-step)| \times \frac{S_L}{2} \\ + |f(i,j) - f(i,j+step)| \times \frac{S_R}{2} \end{array} \right\} \end{cases} \tag{3}$$

In (3), $\Delta f(X_U)$ and $\Delta f(X_D)$ denote the horizontal gradient differences; $\Delta f(Y_L)$ and $\Delta f(Y_R)$ denote the vertical gradient differences; S_U, S_D and S_L, S_R are the horizontal and vertical diffusion functions, respectively; t is the limiting constant; K is the stopping parameter; $GD(X)$ denotes the anisotropic gradient difference regularization factor; and the other variables are defined above.

Let C_iX denote the product of the degree of dispersion in the four directions at pixel i and the value of the spread function in the corresponding direction, C_i represents the gradient operator at i, where X is converted to a column vector. Thus the following equation can be obtained:

$$GD(X) = \sum_{i} \|C_iX\|_1 \tag{4}$$

III. GDR-PCD MODEL

In general, the infrared image containing the target comprises three parts: background, target, and noise images, which can be represented by an additive relationship between them as shown in the following equation:

$$I_D(x,y) = I_T(x,y) + I_B(x,y) + I_N(x,y) \tag{5}$$

In (4), I_D, I_T, and I_B represent the original, target, and background images, respectively, I_N represents the noise image, and (x,y) represents the position of the image element. For example, in the literature [14], an IPI model was proposed for the characteristics of highly correlated backgrounds and sparse targets in local image block,., which constructs the corresponding block images D, T, B, and N for the original image, target image, background image, and noise image, respectively, and obtains the expression of the model as follows:

$$D = B + T + N \tag{6}$$

and the model constraints are as follows:

$$\min_{B,T} \|B\|_* + \lambda \|T\|_1, \quad s.t \ \ \|I - B - T\|_F \le \sigma \tag{7}$$

The $\|\cdot\|_*$ in (6) represents the nuclear norm (sum of singular values), $\|\cdot\|_1$ represents the L1 norm, $\|\cdot\|_F$ represents the Frobenius norm, the λ positive weight constant, and the σ noise level of the image. The literature [15] adds full variance to the background for constraint based on the IPI model more accurately detect the dim and small targets. It proposes a total variance-IPI model based on the total variance-IPI model, which is expressed as follows:

$$\begin{aligned} \min_{B,T} \quad & \|B\|_* + \lambda_1 TV(B) + \lambda_2 \|T\|_1, \\ s.t. \quad & I = T + B + N, \quad \|N\|_F \le \sigma \end{aligned} \tag{8}$$

where TV denotes the TV norm, and in the image $X \in R^{m\times n}$, the TV norm expression is as follows:

$$\begin{aligned} TV(X) = & \sum_{i=1}^{m-1}\sum_{j=1}^{n-1} \sqrt{(X_{i,j} - X_{i+1,j})^2 + (X_{i,j} - X_{i,j+1})^2} \\ & + \sum_{i=1}^{m-1} |X_{i,n} - X_{i+1,n}| + \sum_{j=1}^{n-1} |X_{m,j} - X_{m,j+1}| \end{aligned} \tag{9}$$

The total variance-IPI model can preserve the image edge features and avoid blurring the background in scenes. In this paper, an anisotropic filtering algorithm is used to suppress the infrared image background based on the IPI model and a GDR-PCD model is proposed. The expression of the model is as follows:

$$\min_{B,T} \quad \|A\|_* + \lambda_1 GD(A) + \lambda_2 \|E\|_1,$$

$$s.t. \quad D = E + A + N, \quad \|E\|_F \le \sigma \tag{10}$$

where D, E, A and N represent the original image, target image, background image and noise image respectively, the $\|\cdot\|_*$ represents the nuclear norm (sum of singular values), the $\|\cdot\|_1$ represents the L1 norm, the $\|\cdot\|_F$ is the Frobenius norm, $GD(\cdot)$ denotes the gradient difference regularization factor and the expression is shown in (3), σ represents the noise level of the image, λ_1 and λ_2 is a positive weight constant. Thus, the detection algorithm based on the GDR-PCD model can better preserve the edges and mutated regions than the two previous algorithms and can well suppress the influence of noise in the original image on the target image to get better detection results. The flow chart of the algorithm in this paper is shown in Fig. 4.

IV. OPTIMIZATION ALGORITHM

To simplify the computational process, the complex function optimization problem is combined with the solution ideas from the literature [23], [25] to optimize multiple sub-problems in the process of solving. Equation (9) can be translated into:

$$\begin{aligned} \min_{B,T} \quad & \|M_1\|_* + \lambda_1 \sum_i \|m_i\|_1 + \lambda_2 \|M_3\|_1 \\ s.t. \quad & M_1 = A \\ & M_2 = [m_1; m_2; \ldots; m_{mn}]\, m_i = C_i A \\ & M_3 = E \\ & D = E + A + N, \quad \|N\|_F \le \sigma \end{aligned} \tag{11}$$

Its augmented Lagrangian function is given by:

$$\begin{aligned} L_f = {} & \|M_1\|_* + \lambda_1 \sum_i \|M_i\|_1 + \lambda_2 \|M_3\|_1 + \langle Z_1, M_1 - A\rangle \\ & + \frac{\gamma}{2}\|M_1 - A\|_F^2 + \sum_i \\ & \times (\langle Z_2, M_i - C_i A\rangle + \frac{\gamma}{2}\|M_i - C_i A\|_F^2) \\ & + \langle Z_3, M_3 - E\rangle + \frac{\gamma}{2}\|M_3 - E\|_F^2 \\ & + \langle Z_4, D - E - A - N\rangle \\ & + \frac{\gamma}{2}\|D - A - E - N\|_F^2 \end{aligned} \tag{12}$$

where: γ denotes the penalty factor, $\langle\cdot\rangle$ denotes the inner product of the matrix, $Z_i (i = 1, 2, 3, 4)$ denotes the Lagrange multiplier, where $Z_i\,(i = 1, 3, 4)\,, Z_2 = [y_1, y_2, \ldots, y_{mn}] \in R^{2\times mn}$, and C_i represents the gradient operator at i. To solve the GDR-PCP model, the overlapping directional multiplier method is used in this study [26], [27], which treats the solution problem of each parameter as a sub-problem. In the process of optimizing the parameters, it first fixes other parameters and then optimizes them via multiple iterations, and so on for each parameter in a cycle; eventually, the optimal solution of the whole problem can be obtained.

In solving the problem for the sub-problem on $M_i (i = 1, 2, 3)$, in k + 1 iterations, the sub-problem on M_1 can be transformed into:

$$\begin{aligned} M_1^{k+1} &\leftarrow \arg\min_{M_1} L_f(M_1, M_2^k, M_3^k, A^k, E^k, N^k) \\ &= \arg\min_{M_1} \|M_1\|_* + \left\langle Z_1, M_1 - A^k\right\rangle + \frac{\gamma}{2}\left\|M_1 - A^k\right\|_F^2 \\ &= \arg\min_{M_1} \|M_1\|_* + \frac{\gamma}{2}\left\|M_1 - (A^k - \frac{Z_1^k}{\gamma})\right\|_F^2 \end{aligned} \tag{13}$$

The singular value threshold operator is used to solve the above sub-problem [28].

$$M_1^{k+1} = SVT_{\frac{1}{\beta}}(A^k - \frac{Z_1}{\gamma}) \tag{14}$$

In the above equation, x is the singular value threshold operator, which is expressed as follows:

$$\begin{aligned} SVT_\mu(X) &= Udiag\left[(\sigma - \mu)_+\right] V^T \\ (\sigma - \mu)_+ &= \begin{cases} \sigma - \mu & \sigma > \mu \\ 0 & \textbf{otherwise} \end{cases} \end{aligned} \tag{15}$$

In the above equation, $x = Udiag\,[\cdot]\,V^T$ denotes the singular value decomposition of x. Similarly, in k + 1 iterations, the sub-problem of M_2 can be transformed into:

$$\begin{aligned} M_2^{k+1} &\leftarrow \arg\min_{M_2} L_A(M_1^k, M_3^k, A^k, E^k, N^k) \\ &= \arg\min_{M_2} \sum_i \begin{pmatrix} \|M_i\|_1 + \langle Z_i, M_i - C_i A^k\rangle \\ + \frac{\gamma}{2}\|M_i - C_i A^k\|_F^2 \end{pmatrix} \end{aligned} \tag{16}$$

From the literature [29], the following equation can be used to solve the above M_2 sub-problem:

$$m_i = \max\left\{\left\|C_i A^k - \frac{m_i}{\gamma_i}\right\|_1 - \frac{1}{\gamma_i}, 0\right\} \times \frac{(C_i A - \frac{m_i}{\gamma_i})}{\left\|C_i A - \frac{m_i}{\gamma_i}\right\|_1} \tag{17}$$

The sub-problem of M_3 can be expressed as

$$\begin{aligned} M_3^{k+1} &\leftarrow \arg\min_{M_3} L_A(M_1^k, M_2^k, A^k, E^k, N^k) \\ &= \arg\min_{M_3} \lambda_2 \|M_3\|_1 + \frac{\gamma}{2}\left\|M_3 - (E^k - \frac{Z_3^k}{\gamma})\right\|_F^2 \end{aligned} \tag{18}$$

The above sub-problem is solved using the matrix soft threshold operator, which is defined by the equation:

$$S_\tau(t) = \begin{cases} t - \tau & x > \tau \\ t + \tau & x < \tau \\ 0 & \textbf{otherwise} \end{cases} \tag{19}$$

i.e.

$$M_3^{k+1} = S_{\frac{\lambda_2}{\beta}}(E - \frac{Z_3}{\gamma}) \tag{20}$$

For solving N,A,E sub-problems in the sub-problem for N, k + 1 iterations can be expressed by the following equation:

$$N^{k+1} \leftarrow \arg\min_N \left\langle Z_4^k, D - E^k - A^k - N\right\rangle$$

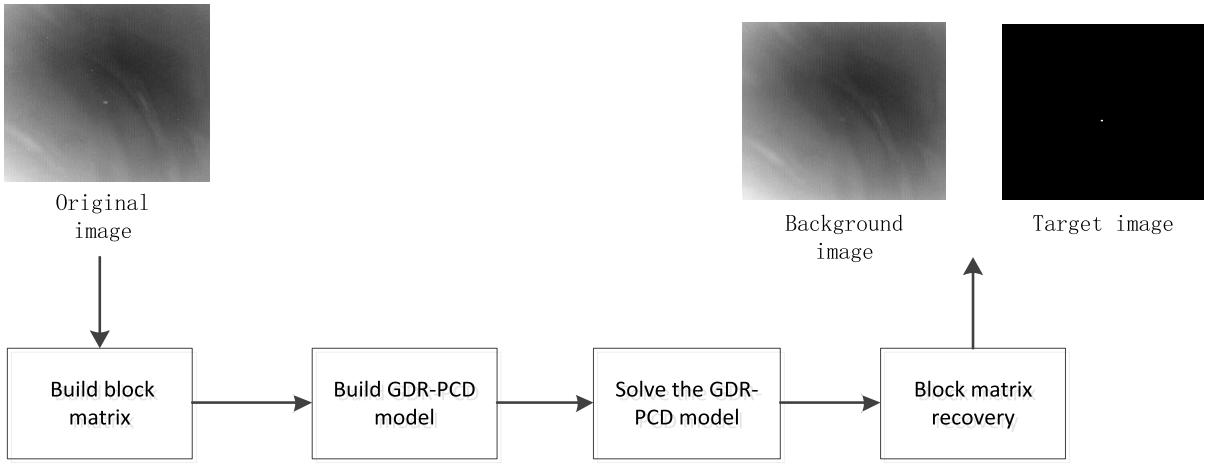

FIGURE 4. Flow chart of the algorithm in this paper.

$$+\frac{\gamma}{2}\left\|D-A^k-E^k-N\right\|_F^2 = \left\|N-(D-A^k-E^k+\frac{Z_4^k}{\gamma})\right\|_F^2, \quad s.t.\ \|N\|_F \le \sigma \tag{21}$$

The solution of the above equation is given by:

$$N^{k+1} = P_\Omega(D-A^k-E^k+\frac{Z_4^k}{\gamma}) \tag{22}$$

where Ω represents the sphere in the three-dimensional space corresponding to $\|\cdot\|_F \le \delta$ and P_Ω represents the projection on this sphere.

For the sub-problem of A, in k + 1 iterations, its solution can be expressed by

$$A^{k+1} \leftarrow \frac{\partial L_f}{\partial A} = 0 \tag{23}$$

The process of solving the above equation is given by:

$$-\frac{\partial L_f}{\partial A} = Z_1^k + Z_4^k + \sum_i \left[C_i^T z_i + \gamma_i C_i^T (m_i - C_i A)\right] + \gamma(M_1^{k+1} - A) + \gamma(D - E^k - N^{k+1}) \tag{24}$$

i.e.

$$A^{k+1} = \left(2\gamma + \sum_i \gamma_i C_i^T C_i\right)^{-1} \cdot \begin{bmatrix} Z_1^k + Z_4^k + \sum_i (C_i^T z_i + \gamma_i C_i^T m_i) \\ +\gamma(M_1^{k+1} + D - E^k - N^{k+1}) \end{bmatrix} \tag{25}$$

For the sub-problem of E, in k + 1 iterations, its solution can be written as:

$$E^{k+1} \leftarrow \frac{\partial L_f}{\partial E} = 0 \tag{26}$$

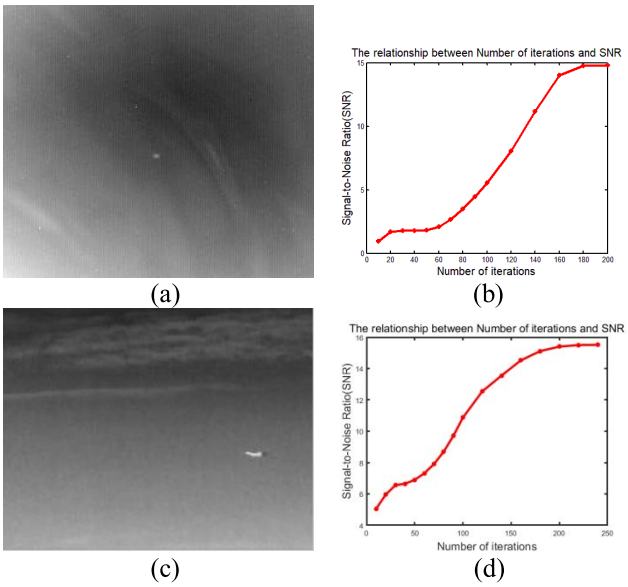

FIGURE 5. (a) and (c) original image of the experiment, (b) and (d) number of iterations versus signal-to-noise ratio.

The result of solving the above equation is:

$$E^{k+1} = \frac{Z_3 + \gamma M_3^{k+1} + Z_4 + \gamma(D - A^k - N^{k+1})}{2\gamma} \tag{27}$$

Finally, the Lagrange multiplier is updated with the following equation:

$$\begin{aligned} Z_1^{k+1} &\leftarrow Z_1^k + \lambda\gamma\left(M_1^{k+1} - A^{k+1}\right) \\ Z_2^{k+1} &\leftarrow Z_2^k + \lambda\gamma\left(M_2^{k+1} - CA^{k+1}\right) \\ Z_3^{k+1} &\leftarrow Z_1^k + \lambda\gamma\left(M_3^{k+1} - E^{k+1}\right) \\ Z_4^{k+1} &\leftarrow Z_4^k + \lambda\gamma\left(D - E^{k+1} - A^{k+1} - N^{k+1}\right) \end{aligned} \tag{28}$$

The above equation (where $\lambda > 0$) is the preset search step and γ denotes the penalty factor; it is the method for solving the GDR-PCD model, which can effectively solve the above model and as well as other similar models. The algorithm specific pseudo code is as follows:

Algorithm 1 Solving Algorithm to GDR-PCD Model.

Input patch-image matrix $D \in \mathrm{R}^{m*n}$, parameters $\lambda_1, \lambda_2, \sigma$
Initialize $M_1^k, M_2^k, M_3^k, Z_1^k, Z_2^k, Z_3^k, Z_4^k, A^k, E^k, N^k$
max-Iter $= 500$, $tol = 5 \times 10^{-10}$,
Output A, E, D
1. while not converged do
2. Fixed other parameters and update M_1^k by

$$M_1^{k+1} = \arg\min_{M_1} \|M_1\|_* + \frac{\gamma}{2} \left\| M_1 - (A^k - \frac{Z_1^k}{\gamma}) \right\|_F^2$$

3. Fixed other parameters and update M_2^k by

$$M_2^{k+1} = \arg\min_{M_2} \sum_i \begin{pmatrix} \|M_i\|_1 + \langle Z_i, M_i - C_i A^k \rangle \\ + \frac{\gamma}{2} \|M_i - C_i A^k\|_F^2 \end{pmatrix}$$

5. Fixed other parameters and update M_3^k by

$$M_3^{k+1} = \arg\min_{M_3} \lambda_2 \|M_3\|_1 + \frac{\gamma}{2} \left\| M_3 - (E^k - \frac{Z_3^k}{\gamma}) \right\|_F^2$$

6. Fixed other parameters and update A^k by

$$A^{k+1} = \left(2\gamma + \sum_i \gamma_i C_i^T C_i \right)^{-1} \cdot \begin{bmatrix} Z_1^k + Z_4^k + \sum_i (C_i^T z_i + \gamma_i C_i^T m_i) \\ + \gamma (M_1^{k+1} + D - E^k - N^{k+1}) \end{bmatrix}$$

7. Fixed other parameters and update E^k by

$$E^{k+1} = \frac{Z_3 + \gamma M_3^{k+1} + Z_4 + \gamma (D - A^k - N^{k+1})}{2\gamma}$$

8. Update the parameter Z_i $(i = 1, 2, 3, 4)$
9. Check the convergence conditions
$\frac{\|D - E^k - A^k - N^k\|_F}{\|D\|_F} < tol$ or $Iter > max - Iter$
10. Iter = Iter+1
11. end while

V. RESULTS AND ANALYSIS

In this section, the algorithm's effectiveness in this paper will be validated through extensive experiments in terms of background recovery in various scenes, noise suppression, and target enhancement. To avoid experimental chance, this paper compares six different scenarios and seven advanced algorithms.

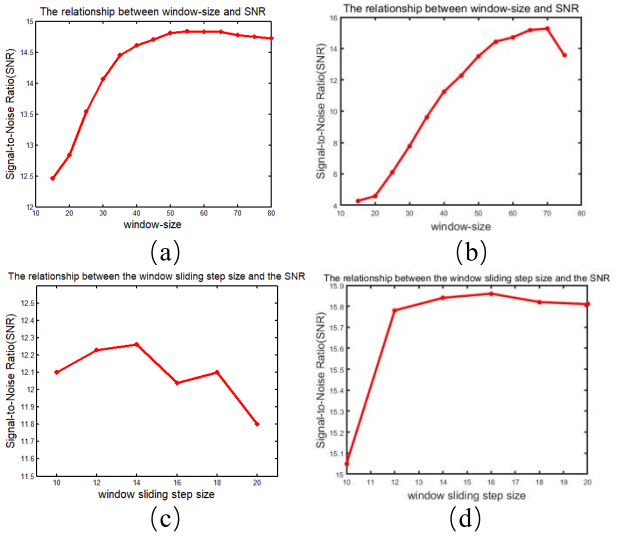

FIGURE 6. (a) and (b) Relationship between window size and SNR, (c) and (d) SNR and window sliding step.

TABLE 1. Description of the experimental scenario.

Scene	Image size	Target size	Target motion trajectory description
1	320*240	3*3	The target moves from the upper right to the middle.
2	320*240	2*10	Target moves from left to right in the middle of the image.
3	278*246	2*2	Target spiral movement in the middle of the image.
4	257*201	3*3	Target moves from left to right in the middle of the image.
5	257*201	1*9	The target is moving to the right of the image towards the middle
6	278*246	3*3	The target is always in the middle of the image

A. PARAMETER ANALYSIS AND SETTING

Several important parameters in the preceding GDR-PCD model have a considerable impact on model performance. In this section, a thorough analysis of the impact of various parameters is conducted on the model and the results are validated through experiments.

B. NUMBER OF ITERATIONS

In the process of solving the GDR-PCD model, by fixing one parameter and finding another parameter that minimizes the objective function, all the parameters in the model are continuously and alternately updated through iterations to

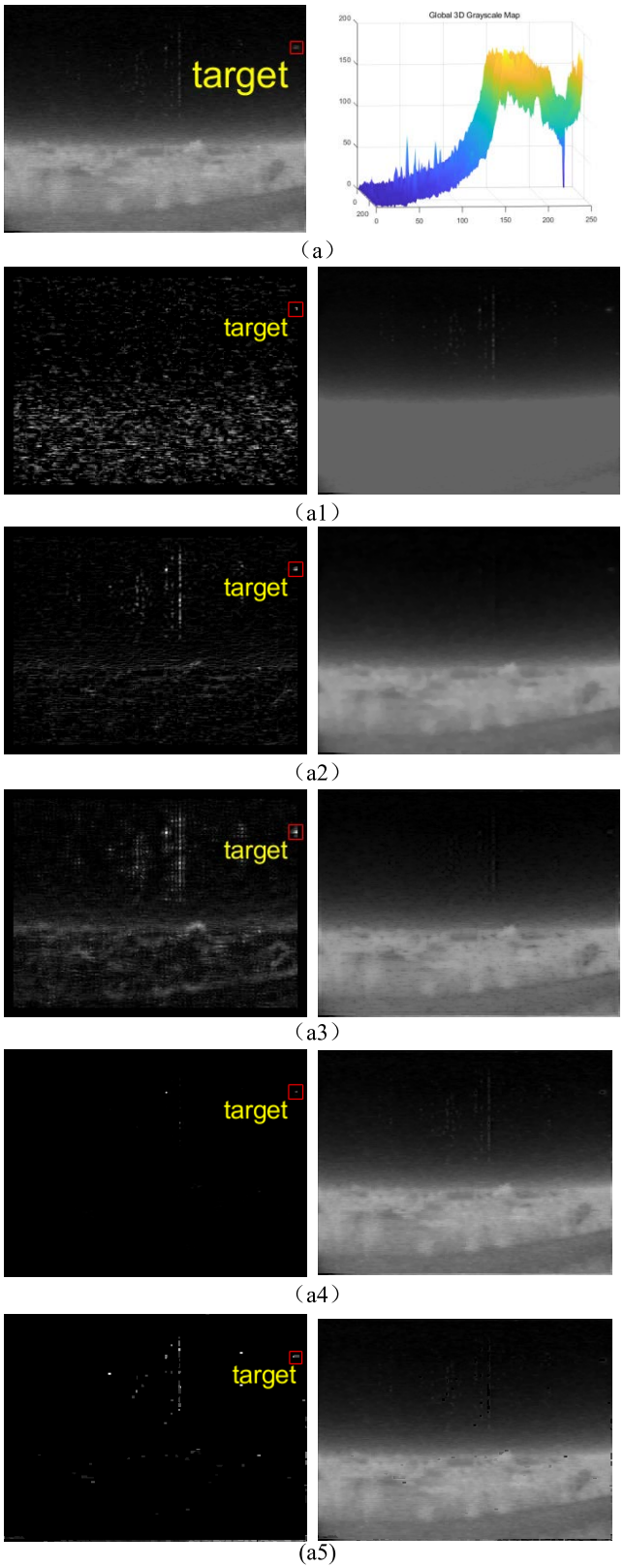

FIGURE 7. (a) Original image of sequence 1, and the corresponding 3D map of this original image; (a1)–(a8) are the difference maps and background prediction maps obtained using the RPCA, top_hat, improved anisotropy, GST, FKRW, PSTNN, TV-PCP, and the algorithm of this paper, respectively.

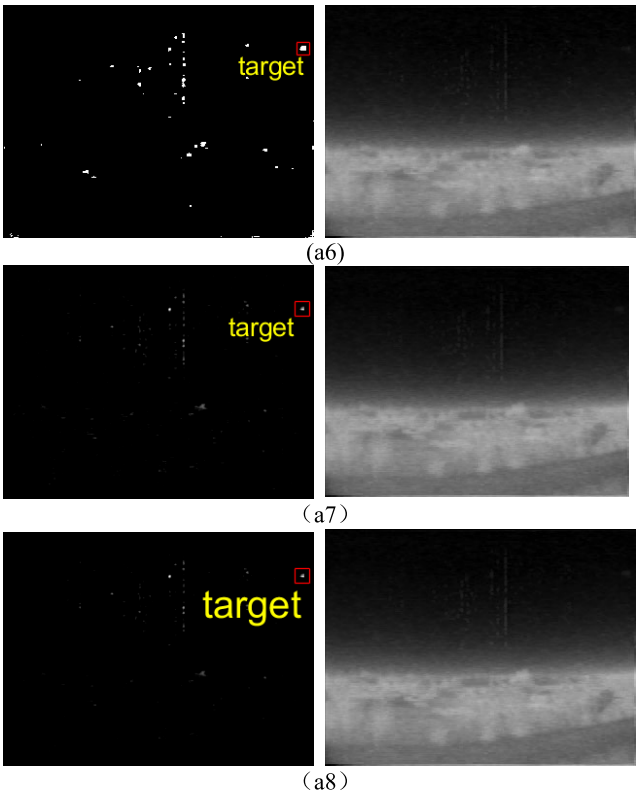

FIGURE 7. *(Continued.)* (a) Original image of sequence 1, and the corresponding 3D map of this original image; (a1)–(a8) are the difference maps and background prediction maps obtained using the RPCA, top_hat, improved anisotropy, GST, FKRW, PSTNN, TV-PCP, and the algorithm of this paper, respectively.

find the optimal solution of the model, and the relationship between the SNR and number of iterations is experimentally plotted in (Fig. 5).

Within a certain range of iterations (Fig. 5), as the number of iterations increases, each parameter of the model approaches the optimal local solution; thus, the SNR increases with more iterations and the gain is larger; however, when the number of iterations increases to a certain extent, each parameter of the model reaches the optimal local solution, and the position behind the curve tends to smooth out. Thus, the SNR no longer increases with the increase in the number of iterations. In this paper, after many experimental investigations, the best result is obtained using 250 iterations.

C. WINDOW SIZE AND SLIDING STEP

To construct a block image matrix, the whole image is traversed through a sliding window with a fixed step size. Then all the data in the sliding window is formed into a column vector, and the resulting column vectors are constructed into the block image matrix. Therefore, the sizes of the sliding window and sliding step of the window considerably affect the construction of the matrix. In this paper, the relationship

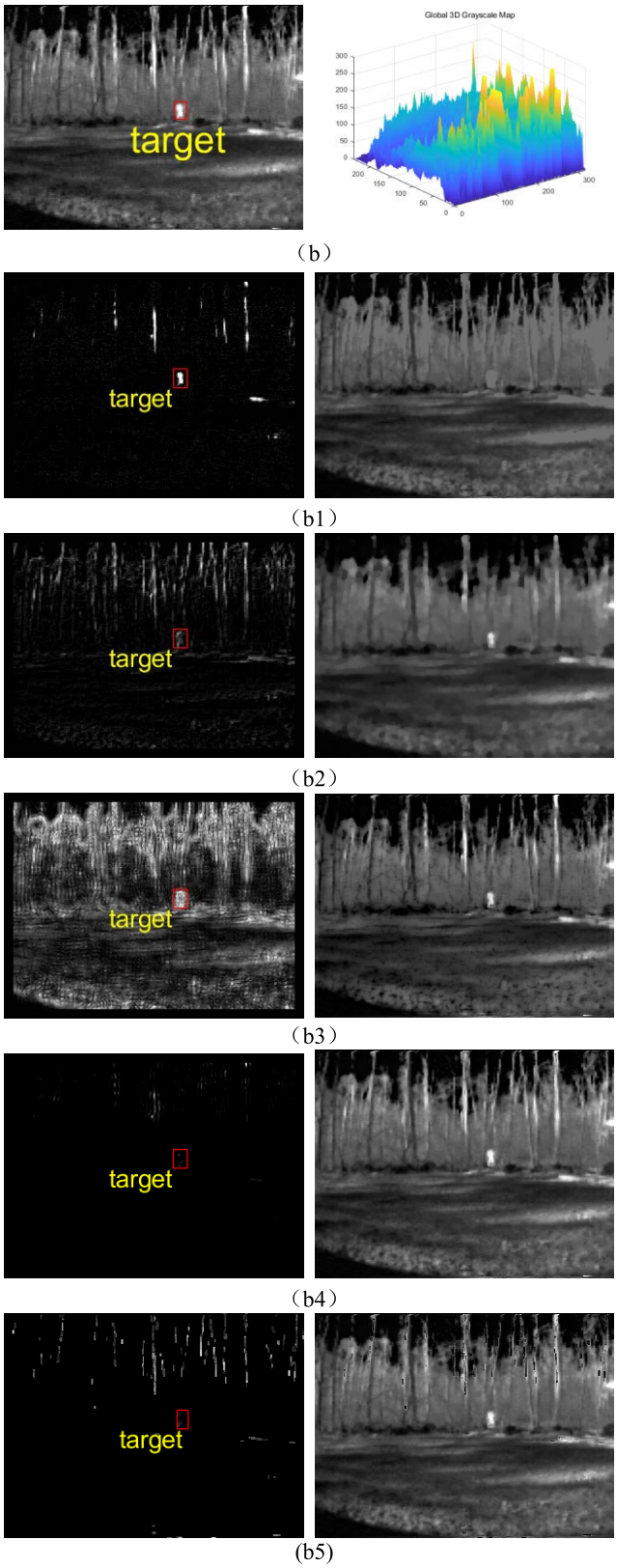

FIGURE 8. (b) Original image of sequence 2, and the corresponding 3D map of this original image; (b1)–(b8) are the difference maps and background prediction maps obtained using the RPCA, top_hat, improved anisotropy, GST, FKRW, PSTNN, TV-PCP, and the algorithm of this paper, respectively.

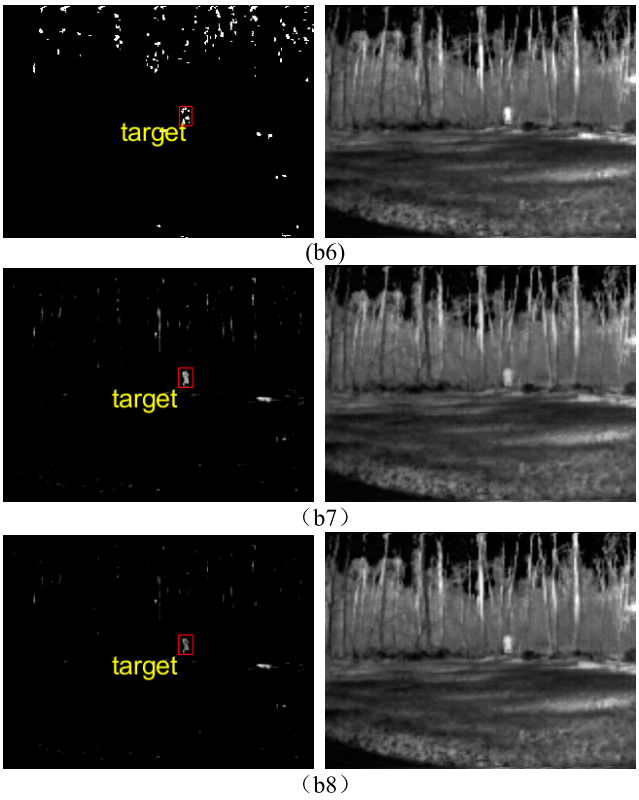

FIGURE 8. *(Continued.)* (b) Original image of sequence 2, and the corresponding 3D map of this original image; (b1)–(b8) are the difference maps and background prediction maps obtained using the RPCA, top_hat, improved anisotropy, GST, FKRW, PSTNN, TV-PCP, and the algorithm of this paper, respectively.

curves of SNR and sliding window size and the relationship curves of SNR and window sliding step are shown in Fig. 6.

As shown in Fig. 6, when the sliding window is within a certain range, the SNR increases with the increase in the sliding window size because when the sliding window size increases, the more neighbor information is contained in each window, but when the sliding window size exceeds a certain range, SNR decreases with the increase in the sliding window size because after the sliding window exceeds a certain range, the larger the window, the included region is expanded from the smooth region to the non-smooth region, the low-rank property of the composed column vectors will be obsolete when the sliding window exceeds a certain range; thus, the SNR decreases. The smaller the overlap between the data blocks, the better is the local correlation between the blocks and the better it is for preserving the low-rank characteristics of the data matrix as the sliding step size of the window increases from small to large; as the step size increases, no overlap area exists between the data blocks, and the local autocorrelation decreases, especially when the smooth background area enters the non-stationary edge contour area, which will greatly reduce the low-rank characteristics of the data. After conducting numerous experiments, the best result is obtained when the window size is 65×65 and the sliding step length is 14.

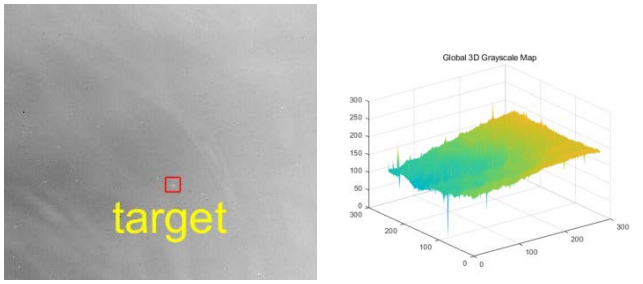

(c)

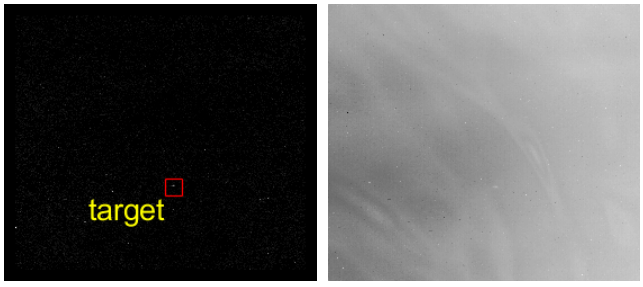

(c1)

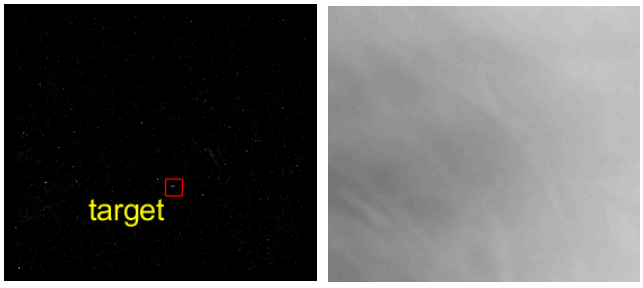

(c2)

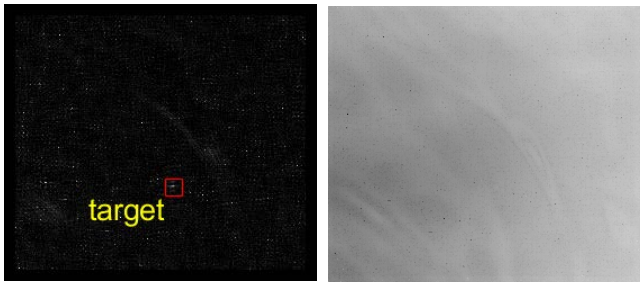

(c3)

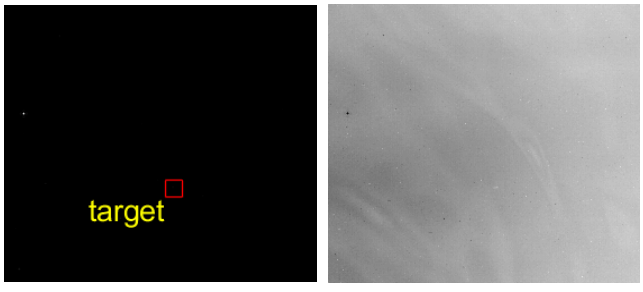

(c4)

FIGURE 9. (c) Original image of sequence 3, and the corresponding 3D map of this original image; (c1)–(c8) are the difference maps and background prediction maps obtained using the RPCA, top_hat, improved anisotropy, GST, FKRW, PSTNN, TV-PCP, and the algorithm of this paper, respectively.

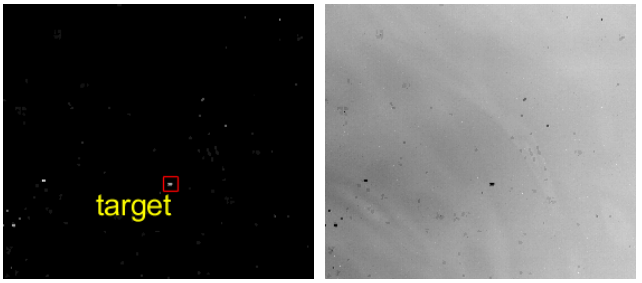

(c5)

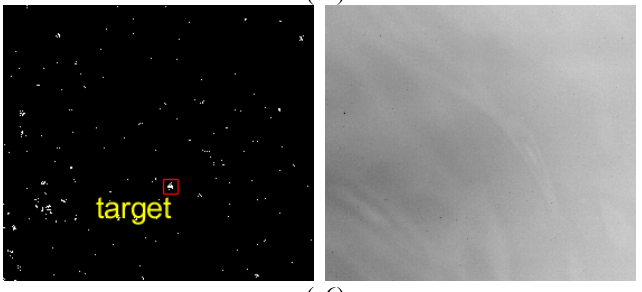

(c6)

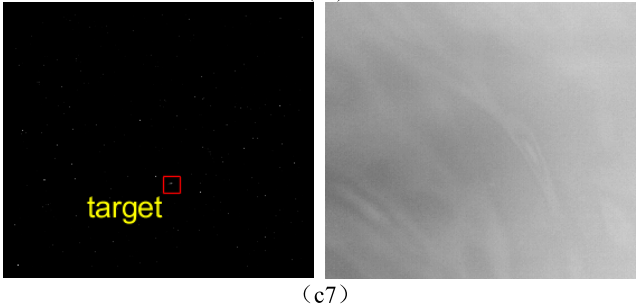

(c7)

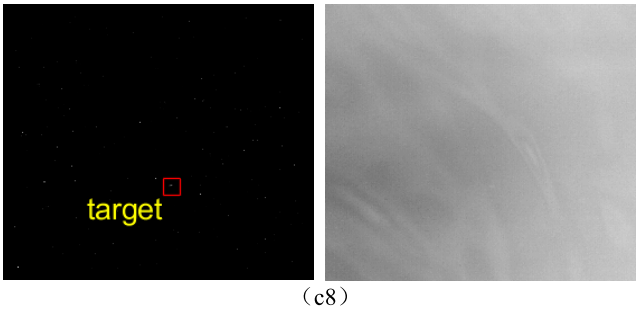

(c8)

Continued. **FIGURE 9.** (c) Original image of sequence 3, and the corresponding 3D map of this original image; (c1)–(c8) are the difference maps and background prediction maps obtained using the RPCA, top_hat, improved anisotropy, GST, FKRW, PSTNN, TV-PCP, and the algorithm of this paper, respectively.

D. INTRODUCTION TO THE EXPERIMENTAL SCENES

In this paper, the effectiveness of the algorithm is verified by different scenarios, and each sequence is described as shown in Table 1.

E. TEST RESULTS AND ANALYSIS

In this study, to evaluate the effectiveness of the algorithm, the infrared images of the above six scenes are tested and compared with seven classical algorithms in the line, namely,

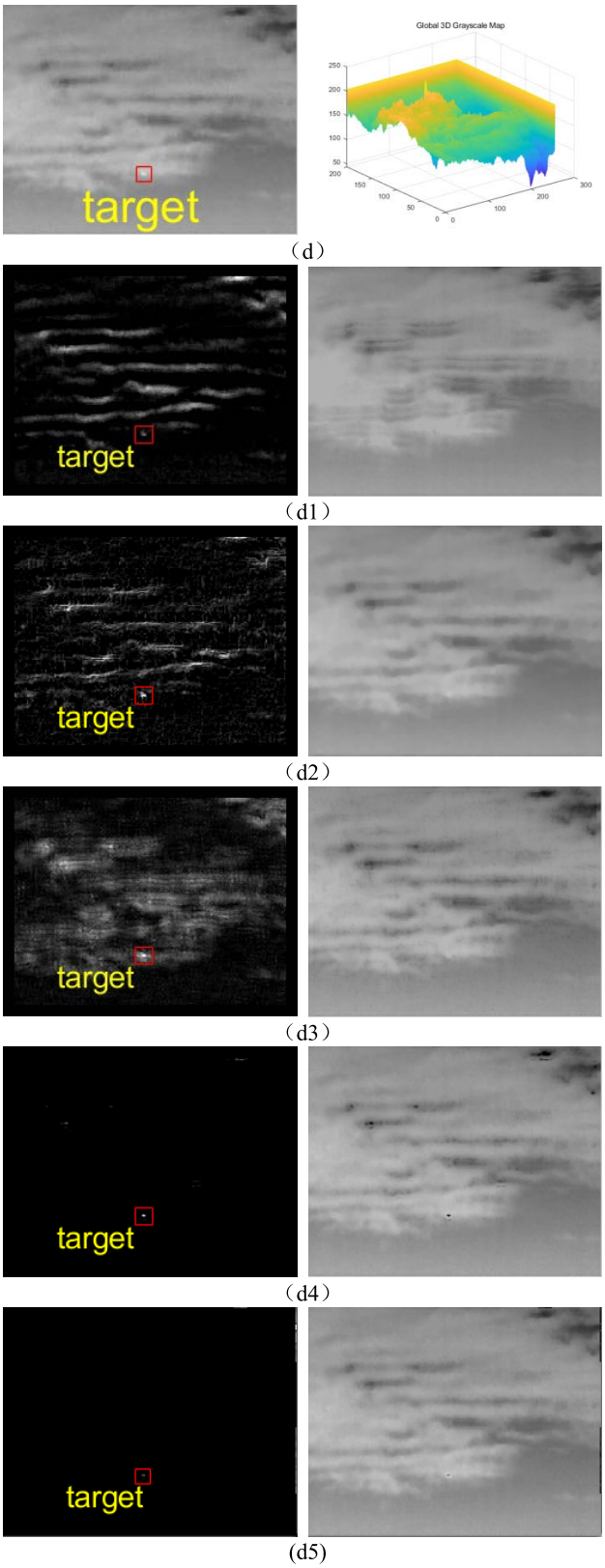

FIGURE 10. (d) Original image of sequence 4, and the corresponding 3D map of this original image; (d1)–(d8) are the difference maps and background prediction maps obtained using the RPCA, top_hat, improved anisotropy, GST, FKRW, PSTNN, TV-PCP, and the algorithm of this paper, respectively.

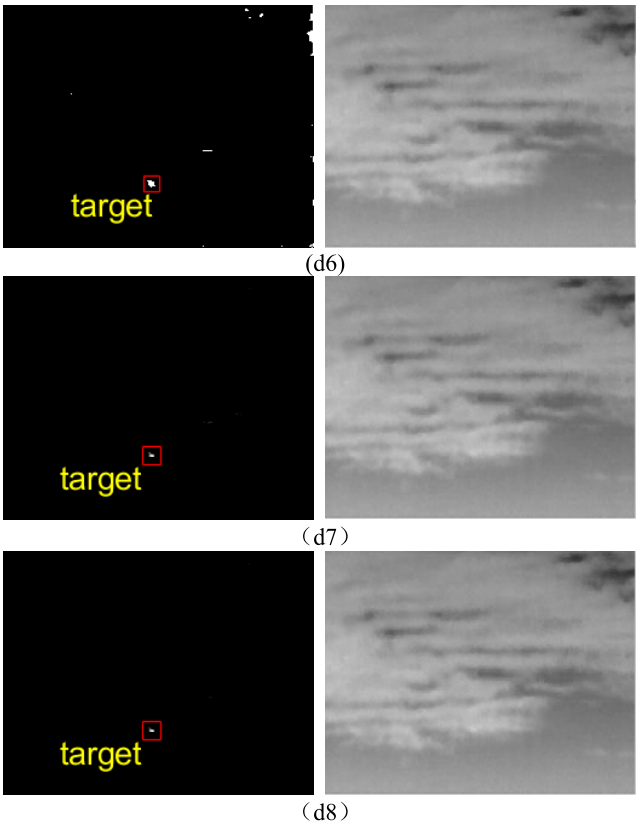

FIGURE 10. *(Continued.)* (d) Original image of sequence 4, and the corresponding 3D map of this original image; (d1)–(d8) are the difference maps and background prediction maps obtained using the RPCA, top_hat, improved anisotropy, GST, FKRW, PSTNN, TV-PCP, and the algorithm of this paper, respectively.

the robust principal component analysis algorithm (RPCA), improved top-hat filtering algorithm (top-hat), improved various anisotropy filtering algorithm, generalized structure tensor algorithm (GST) [30], FacetKernel and Random Walker algorithm (FKRW) [31], Partial Sum of the tensor nuclear norm algorithm(PSTNN) [32] and the TV-PCP algorithm. In this study we show the original images of six scenes and the 3D maps corresponding to the original images and the different maps and background prediction images obtained using the five classical algorithms and the algorithm proposed in this paper.

The RPCA combines multi-frame information to decompose sparse target and low-rank background images from the original image matrix, as shown in Fig. 7- Fig. 12. However, the presence of clutter is not considered in the algorithm model, resulting in the presence of large areas of bright background information in the difference maps obtained for bright background sequence images. Improved top-hat filtering algorithm uses open and closed operations combined with kernel matrix implementation to model the background of the original image and finally obtains the difference map, but it eliminates most of the noise in the process of open and closed

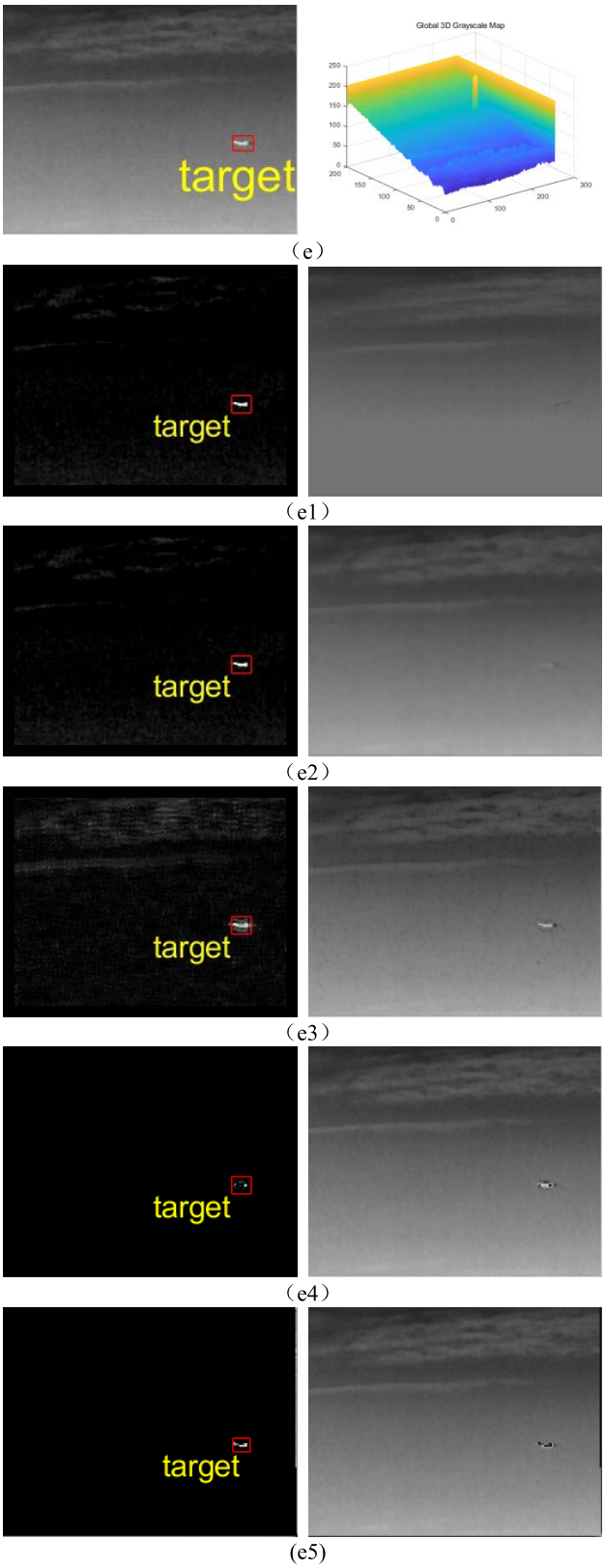

FIGURE 11. (e) Original image of sequence 5, and the corresponding 3D map of this original image; (e1)–(e8) are the difference maps and background prediction maps obtained using the RPCA, top_hat, improved anisotropy, GST, FKRW, PSTNN, TV-PCP, and the algorithm of this paper, respectively.

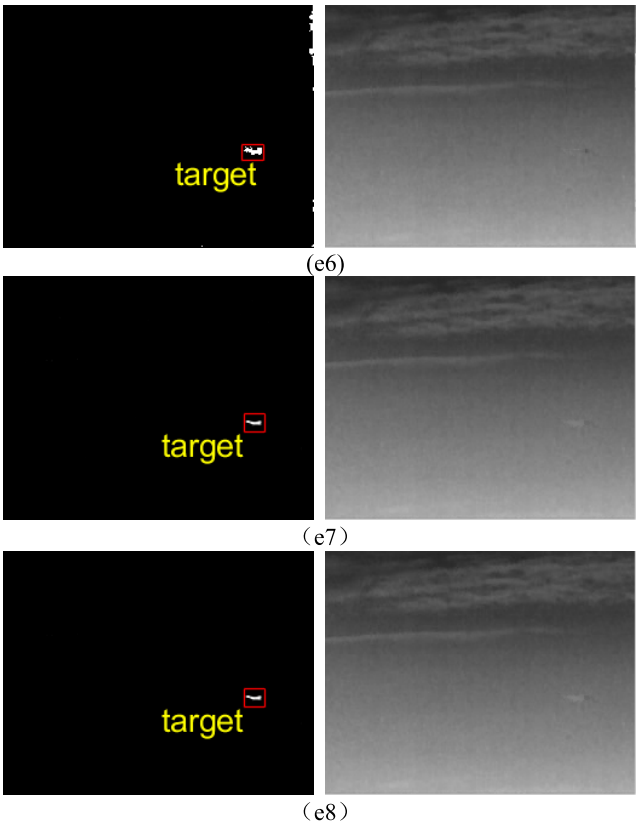

FIGURE 11. *(Continued.)* (e) Original image of sequence 5, and the corresponding 3D map of this original image; (e1)–(e8) are the difference maps and background prediction maps obtained using the RPCA, top_hat, improved anisotropy, GST, FKRW, PSTNN, TV-PCP, and the algorithm of this paper, respectively.

operations. The energy intensity of the target point is affected during the open and closed operations, resulting in a dim and small target of the difference map that is not obvious. The anisotropic filtering algorithm predicts the central image element by combining the domain information to remove noise from the background image, but it cannot effectively suppress large areas of noise and clutter. Simultaneously, the energy of the target point is affected in the process of removing noise, which leads to the detection target of the difference map being not obvious. The GST algorithm achieves infrared target detection using the second-order conjugate symmetric derivative of 2D Gaussian, which can effectively suppress the noise and bright background in the original image, but it loses the information of dim and small targets in filtering, making the target incomplete in the difference map. The FKRW algorithm first removes the small noise by filtering, and then enhances the target signal and suppresses the clutter by local contrast descriptors, however, the algorithm will cause the loss of target energy when filtering the original image under the complex striped background, and cannot fully recover the target signal when enhancing it later, leading to the loss of the target contour in the detection results. The

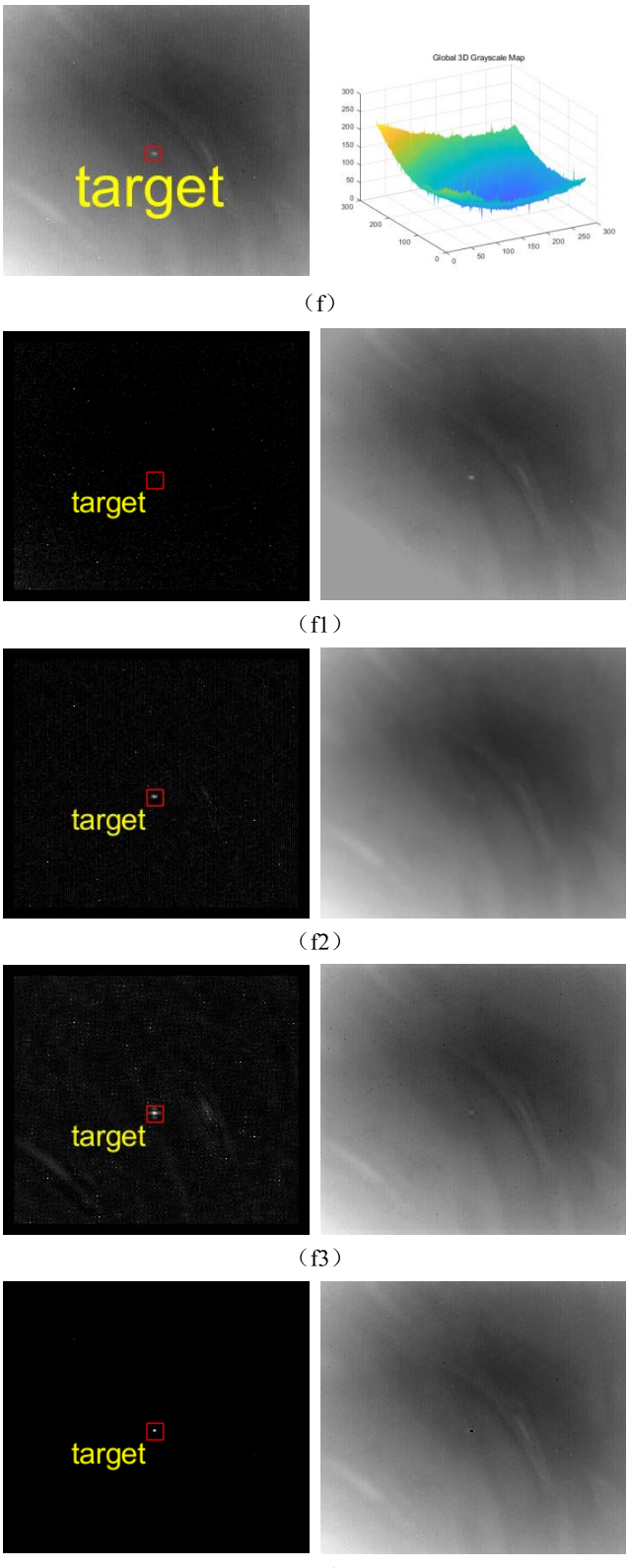

FIGURE 12. (f) Original image of sequence 6, and the corresponding 3D map of this original image; (f1)–(f8) are the difference maps and background prediction maps obtained using the RPCA, top_hat, improved anisotropy, GST, FKRW, PSTNN, TV-PCP, and the algorithm of this paper, respectively.

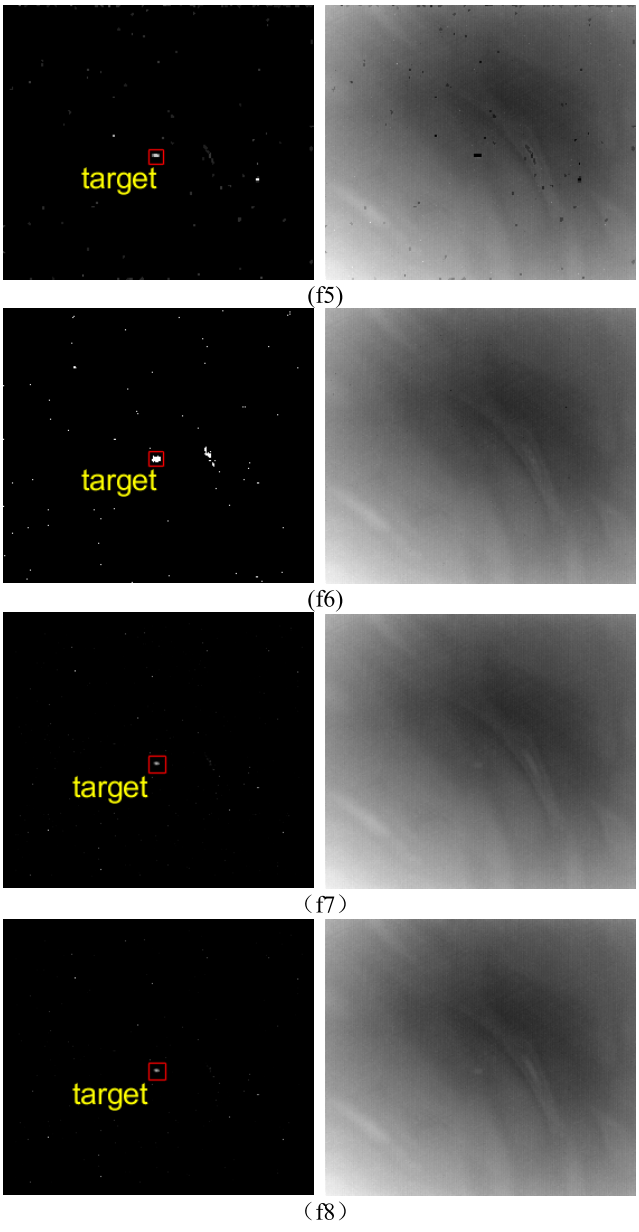

FIGURE 12. (f) Original image of sequence 6, and the corresponding 3D map of this original image; (f1)–(f8) are the difference maps and background prediction maps obtained using the RPCA, top_hat, improved anisotropy, GST, FKRW, PSTNN, TV-PCP, and the algorithm of this paper, respectively.

PSTNN algorithm achieves the purpose of suppressing the background and preserving the target by using the partial sum of tensor nuclear norm and weighted L1 norm, however, when the algorithm contains many small noises in the image, partial sum of tensor nuclear norm is not ideal for constraining the background image, resulting in many noises in the final target image. The TV-PCP algorithm predicts the background image using the IPI model's block matrix idea, whereas the TV-parametric constrains the background image.

However, the TV-parametric does not effectively preserve the edge contour regions and noise in the complex image when constraining the background image, resulting in numerous noise and edge contours in the final differential image. The algorithm proposed in this paper implements the prediction of background images using the IPI model. Further, it proposes the gradient difference regularization factor; the background is constrained by this regularization factor, which can effectively remove the edge contour region and noise, improving the difference map.

Moreover, to evaluate the detection effect of the algorithm, three evaluation metrics are introduced in this paper, structural similarity (SSIM) [33], background suppression factor (BSF), and SNR. SSIM mainly evaluates the magnitude of the similarity between the background image predicted by the algorithm and the original image, which is calculated as follows

$$SSIM = \frac{(2\mu_R\mu_F + \varepsilon_1)(2\sigma_{RF} + \varepsilon_2)}{(\mu_R^2 + \mu_F^2 + \varepsilon_1)(\sigma_R^2 + \sigma_F^2 + \varepsilon_2)} \tag{29}$$

where μ_R and σ_R are the mean and standard deviation of the original image, respectively; μ_F and σ_F are the mean and standard deviation of the predicted images, respectively; σ_{RF} is the covariance of the original image and predicted background image; ε_1 and ε_2 are constants, typically 0.01. BSF is mainly used to evaluate the effect of the background image predicted by the algorithm by differencing the image and original image, which is calculated as follows:

$$BSF = \sigma_{in}/\sigma_{out} \tag{30}$$

where σ_{in} and σ_{out} are the mean squared differences between the input image and the difference image, respectively. The SNR can be used to evaluate the contrast between the target and the noise energy obtained by the algorithm and thus verify the detection effect of the algorithm, which is calculated as follows:

$$SNR = 10 \times \log_{10}^{(A_E - A_B)/\sigma_B} \tag{31}$$

where A_E is the mean value of the target region; A_B is the mean value of the background region; and σ_B is the standard deviation of the background region.

Table.2 shows that the algorithm proposed in this paper has larger values of structural similarity SSIM and BSF in different scenes compared with the other five algorithms; the SNR is still larger in different sequences compared with other algorithms, which proves that the algorithm proposed in this paper has a greater advantage in target detection. In sequence three the evaluation index is not the maximum but very close to the maximum.

To comprehensively evaluate the performance of this algorithm and other five algorithms, this study draws an operating test curve (ROC) using detection rate and false alarm rate, and the ROC curve is used to comprehensively evaluate this algorithm and other five algorithms. The detection rate and false alarm rate are calculated as follows:

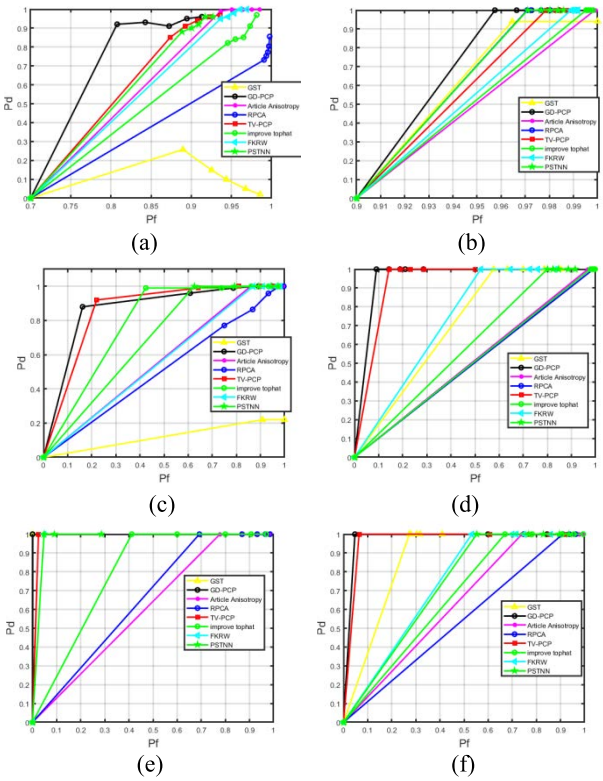

FIGURE 13. ROC curves of different algorithms for six scenes.

The ROC curves of the six scenes (Fig. 13) show that the algorithm proposed in this paper uses the gradient difference regularization factor to further constrain the background based on the IPI model, which can achieve noise removal and obtain good background estimation and detection. Fig. 13(a) shows that when Pf = 0.8, the detection rate of the algorithm in this study is at 85%, whereas the detection rates of other algorithms are <50%, indicating that the algorithm proposed in this paper can maintain good detection performance in the case of large-area clutter and more noise around the target signal. Fig. 13(b) shows that when the target is large and the surrounding clutter is similar to that of the target, the algorithm proposed in this paper can still maintain a good detection performance. Fig. 13(c) shows that at Pf = 0.15, the Pd of this algorithm is approximately 90%, whereas the Pd of all other algorithms is <70%, indicating that this algorithm is good for background estimation in the case of small differences in the mean values of clutter and target signal intensity. Fig. 13(d) shows that at Pf = 0.1, The Pd of the algorithm in this paper is around 100%, and the Pd of TV-PCP = 75%, while the Pd of the rest of the algorithms is below 20%, which indicates that when the target is submerged in the clouds, the algorithm in this paper can eliminate the clouds around the target and thus preserve the target signal. In Fig. 13(e), this algorithm Pd is always kept at 100%. In Fig. 13(f) at Pf <0.1, both this algorithm and TV-PCP algorithm Pd can reach 100%, indicating that this algorithm has a good detection effect when the target is located under bright and empty scene with a dim textured background. The above comprehensive

TABLE 2. Evaluation index values of various algorithms.

	Evaluation indicators	Seq1	Seq2	Seq3	Seq4	Seq5	Seq6
Top_hat	SSIM	0.9955	0.9116	0.9875	0.9479	0.9745	0.9949
	BSF	122.4546	26.7856	75.7493	31.6858	45.3859	116.9671
	SNR	-10.83	2.57	6.82	4.21	9.19	10.48
RPCA	SSIM	0.9996	**0.9989**	0.9987	0.9711	0.9935	0.9998
	BSF	27.7416	29.1549	66.7014	23.8678	19.9365	36.9551
	SNR	-15.62	-1.92	0.49	12.85	11.98	-10.34
Improved anisotropy algorithm	SSIM	0.9961	0.9538	0.9945	0.9837	0.9972	0.998
	BSF	168.4711	44.1131	95.5877	54.0696	145.4731	183.3438
	SNR	**-0.8**	2.12	6.78	7.71	10.38	11.74
GST	SSIM	**0.9999**	0.9974	**0.9996**	0.9905	0.9981	0.9995
	BSF	397.5986	130.2289	189.2198	57.7251	152.5916	214.9049
	SNR	-5.9	-0.39	4.58	14.74	7.26	14.18
FKRW	SSIM	0.998	0.985	0.9966	0.9989	0.9966	0.9992
	BSF	202.7807	56.234	98.2173	181.2476	115.0467	182.5165
	SNR	-10.88	-10.5	11.74	0.5	7.93	14.3
PSTNN	SSIM	0.996	0.9959	0.9986	0.9965	0.9961	0.9995
	BSF	562.3066	111.0320	**194.9203**	124.2767	121.0161	344.7666
	SNR	-12.59	-11.77	**10.42**	12.11	13.58	**15.93**
TV-PCP	SSIM	0.9998	0.9933	0.998	0.9997	0.9986	0.9995
	BSF	476.1468	87.9106	158.5246	415.1057	186.0899	329.3319
	SNR	-2.2	**11.66**	8.39	14.13	14.76	14.93
Proposed method	SSIM	**0.9999**	0.9974	0.9985	**0.9999**	**0.9987**	**0.9997**
	BSF	**667.3514**	**140.8542**	182.8524	**597.2135**	**194.8923**	**380.1446**
	SNR	-1.5	10.39	8.26	**15.52**	**14.85**	15.19

analysis, compared with other algorithms, can be obtained in different practical contexts. The algorithm proposed in this paper can achieve the best detection results.

VI. CONCLUSION

In this paper, we propose a dim and small target detection method combining a multi-way gradient difference regularization principal component decomposition model to establish a new gradient difference regularization factor to constrain the infrared background image by combining the gradient difference between adjacent row and column vectors with a diffusion function; further, we propose a new GDR-PCD model based on the IPI model. The model transforms the dim and small target detection model into a recovery problem with low-rank and sparse matrices and solves the model using the alternating direction multiplier method. After analyzing a large amount of experimental data, we demonstrate that the algorithm proposed in this paper outperforms other traditional algorithms in terms of detection performance and background estimation effect in various practical scenarios. In the future, we will further optimize the algorithm's solution method to improve the algorithm's operation speed; in the meantime, we will continue to consider combining the algorithm with other spatial filtering methods to improve the algorithm's detection performance in complex and variable environments to make it applicable to a wider range of applications.

REFERENCES

[1] Z. Chen, S. Luo, T. Xie, J. Liu, G. Wang, and G. Lei, "A novel infrared small target detection method based on BEMD and local inverse entropy," *Infr. Phys. Technol.*, vol. 66, pp. 114–124, Sep. 2014, doi: 10.1016/j.infrared.2014.05.013.

[2] Y. Chen, B. Song, D. Wang, and L. Guo, "An effective infrared small target detection method based on the human visual attention," *Infr. Phys. Technol.*, vol. 95, pp. 128–135, Dec. 2018, doi: 10.1016/j.infrared.2018.10.033.

[3] Y. Chen, B. Song, X. Du, and M. Guizani, "Infrared small target detection through multiple feature analysis based on visual saliency," *IEEE Access*, vol. 7, pp. 38996–39004, 2019, doi: 10.1109/ACCESS.2019.2906076.

[4] Y. Sun, J. Yang, Y. Long, and W. An, "Infrared small target detection via spatial-temporal total variation regularization and weighted tensor nuclear norm," *IEEE Access*, vol. 7, pp. 56667–56682, 2019, doi: 10.1109/ACCESS.2019.2914281.

[5] I. S. Reed, R. M. Gagliardi, and H. M. Shao, "Application of three-dimensional filtering to moving target detection," *IEEE Trans. Aerosp. Electron. Syst.*, vol. AES-19, no. 6, pp. 898–905, Nov. 1983.

[6] Y. Xie, L. Dong, M. Zhao, and W. Xu, "A small dim infrared maritime target detection algorithm based on local peak detection and pipeline-filtering," presented at the 7th Int. Conf. Graphic Image Process. (ICGIP), 2015.

[7] L. Dong, B. Wang, Z. Ming, and W. Xu, "Robust infrared maritime target detection based on visual attention and spatiotemporal filtering," *IEEE Trans. Geosci. Remote Sens.*, vol. 55, no. 5, pp. 3037–3050, May 2017.

[8] Y. N. Zhang, X. G. Chen, and X. U. Wen-Hai, "High-speed implementation of infrared detection algorithm for weak targets on sea surface," *J. Optoelectron. Laser*, vol. 30, no. 5, p. 6, 2019.

[9] I. S. Reed, R. M. Gagliardi, and L. B. Stotts, "Optical moving target detection with 3-D matched filtering," *IEEE Trans. Aerosp. Electron. Syst.*, vol. 24, no. 4, pp. 327–336, Jul. 1988.
[10] X. Yan, J.-X. Peng, M.-Y. Ding, and D.-H. Xue, "An extended track-before-detect algorithm for infrared target detection," *IEEE Trans. Aerosp. Electron. Syst.*, vol. 33, no. 3, pp. 1087–1092, Jul. 1997, doi: 10.1109/7.599339.
[11] J. Gong, Y. Zhang, Q. Hou, W. He, H. Guan, and W. Zhang, "Background suppression for cloud clutter using temporal difference projection," *Infr. Phys. Technol.*, vol. 64, pp. 66–72, May 2014, doi: 10.1016/j.infrared.2014.01.008.
[12] Q. Guo, Z. Li, W. Song, and W. Fu, "Parallel computing based dynamic programming algorithm of track-before-detect," *Symmetry*, vol. 11, no. 1, p. 29, Dec. 2018, doi: 10.3390/sym11010029.
[13] X. Fan, Z. Xu, J. Zhang, Y. Huang, Z. Peng, Z. Wei, and H. Guo, "Dim small target detection based on high-order cumulant of motion estimation," *Infr. Phys. Technol.*, vol. 99, pp. 86–101, Jun. 2019, doi: 10.1016/j.infrared.2019.04.008.
[14] C. Q. Gao, D. Meng, Y. Yang, Y. Wang, X. Zhou, and A. G. Hauptmann, "Infrared patch-image model for small target detection in a single image," *IEEE Trans. Image Process.*, vol. 22, no. 12, pp. 4996–5009, Dec. 2013, doi: 10.1109/TIP.2013.2281420.
[15] Y. Liu and Z. Peng, "Infrared small target detection based on resampling-guided image model," *IEEE Geosci. Remote Sens. Lett.*, vol. 19, pp. 1–5, 2022.
[16] X. Wang, Z. Peng, D. Kong, and Y. He, "Infrared dim and small target detection based on stable multisubspace learning in heterogeneous scene," *IEEE Trans. Geosci. Remote Sens.*, vol. 55, no. 10, pp. 5481–5493, Oct. 2017.
[17] D. Pang, T. Shan, P. Ma, W. Li, S. Liu, and R. Tao, "A novel spatiotemporal saliency method for low-altitude slow small infrared target detection," *IEEE Geosci. Remote Sens. Lett.*, vol. 19, pp. 1–5, 2022.
[18] Y. Sun, J. Yang, and W. An, "Infrared dim and small target detection via multiple subspace learning and spatial-temporal patch-tensor model," *IEEE Trans. Geosci. Remote Sens.*, vol. 59, no. 5, pp. 3737–3752, May 2021.
[19] B. Zca, K. Xuan, Z. Qiang, B. Sca, and B. Zpa, "Infrared dim target detection via mode-k_1k_2 extension tensor tubal rank under complex ocean environment," *ISPRS J. Photogramm. Remote Sens.*, vol. 181, pp. 167–190, Nov. 2021.
[20] G. Wang, B. Tao, X. Kong, and Z. Peng, "Infrared small target detection using non-overlapping patch spatial–temporal tensor factorization with capped nuclear norm regularization," *IEEE Trans. Geosci. Remote Sens.*, vol. 60, 2021, Art. no. 5001417.
[21] X. Kong, C. Yang, S. Cao, C. Li, and Z. Peng, "Infrared small target detection via nonconvex tensor fibered rank approximation," *IEEE Trans. Geosci. Remote Sens.*, vol. 60, pp. 1–21, 2022.
[22] D. Pang, T. Shan, W. Li, P. Ma, and R. Tao, "Infrared dim and small target detection based on greedy bilateral factorization in image sequences," *IEEE J. Sel. Topics Appl. Earth Observ. Remote Sens.*, vol. 13, no. 99, pp. 3394–3408, Jun. 2020.
[23] X. Wang, Z. Peng, D. Kong, P. Zhang, and Y. He, "Infrared dim target detection based on total variation regularization and principal component pursuit," *Image Vis. Comput.*, vol. 63, pp. 1–9, Jul. 2017, doi: 10.1016/j.imavis.2017.04.002.
[24] Y. H. Wang and W. N. Liu, "Dim target enhancement algorithm for low-contrast image based on anisotropic diffusion," *Opto-Electron. Eng.*, vol. 35, no. 6, pp. 15–19, Jun. 2008.
[25] Y. X. Wang, "Research on the theory and method of infrared dim and small target detection based on sparse dynamic inversion," School Inf. Commun. Eng., Univ. Electron. Sci. Technol., Chengdu, China, 2019.
[26] Z. Wang, H. Li, Q. Ling, and W. Li, "Mixed Gaussian-impulse video noise removal via temporal-spatial decomposition," in *Proc. IEEE Int. Symp. Circuits Syst.*, May 2012, pp. 1851–1854.
[27] G. Chen, J. Zhang, D. Li, and H. Chen, "Robust Kronecker product video denoising based on fractional-order total variation model," *Signal Process.*, vol. 119, pp. 1–20, Feb. 2016, doi: 10.1016/j.sigpro.2015.06.027.
[28] J.-F. Cai, E. J. Candès, and Z. Shen, "A singular value thresholding algorithm for matrix completion," *SIAM J. Optim.*, vol. 20, no. 4, pp. 1956–1982, 2010, doi: 10.1137/080738970.
[29] C. B. Li, "An efficient algorithm for total variation regularization with applications to the single pixel camera and compressive sensing," Dept. Comput. Appl. Math., Rice Univ., Houston, TX, USA, 2011.
[30] C.-Q. Gao, J.-W. Tian, and P. Wang, "Generalised-structure-tensor-based infrared small target detection," *Electron. Lett.*, vol. 44, no. 23, p. 1349, 2008, doi: 10.1049/el:20081781.
[31] Y. Qin, L. Bruzzone, C. Gao, and B. Li, "Infrared small target detection based on facet kernel and random Walker," *IEEE Trans. Geosci. Remote Sens.*, vol. 57, no. 9, pp. 7104–7118, Sep. 2019.
[32] L. Zhang and Z. Peng, "Infrared small target detection based on partial sum of the tensor nuclear norm," *Remote Sens.*, vol. 11, no. 4, p. 382, Feb. 2019.
[33] Z. Wang, A. C. Bovik, H. R. Sheikh, and E. P. Simoncelli, "Image quality assessment: From error visibility to structural similarity," *IEEE Trans. Image Process.*, vol. 13, no. 4, pp. 600–612, Apr. 2004, doi: 10.1109/TIP.2003.819861.

ANQING WU received the bachelor's degree from the Huaihua College, Hunan, China. He was a Graduate Student with the Huaihua College. His research interests include signal processing and image detection and tracking algorithms.

XIANGSUO FAN received the B.S. degree in automation from Hainan Normal University, Haikou, China, in 2012, and the M.S. and Ph.D. degrees from the University of Electronic Science and Technology of China, Chengdu, China, in 2015 and 2019, respectively. Since 2019, he has been an Associate Professor with the School of Electrical and Information Engineering, Guangxi University of Science and Technology, Liuzhou, China. His research interests include signal processing and image detection and tracking algorithms.

HUAJIN CHEN received the B.S. degree from Yulin Normal University, in 2010, the M.S. degree from Zhejiang Normal University, in 2013, and the Ph.D. degree from Fudan University, in 2016. Since 2016, he has been an Associate Professor with the School of Electrical and Information Engineering, Guangxi University of Science and Technology, Liuzhou, China. His research interest includes optical manipulations, image detection, and tracking algorithms.

LEI MIN received the B.S. and M.S. degrees in mathematics from Sichuan University, Chengdu, China, in 2009 and 2012, respectively, and the Ph.D. degree from the University of Electronic Science and Technology of China, Chengdu, in 2019. Since 2019, he has been a Researcher with the Institute of Optics and Electronics, Chinese Academy of Sciences. His research interests include signal processing, image super-resolution, image detection, and tracking algorithms.

ZHIYONG XU was born in Chengdu, Sichuan, China, in 1967. He received the B.S. degrees from Sichuan University and the M.S. degree from the University of Electronic Science and Technology of China. He is currently a Researcher with the Institute of Optics and Electronics, Chinese Academy of Sciences, and the Master Student Supervisor with the University of Chinese Academy of Sciences. His research interests include signal processing and image reconstruction algorithms.